Modelling the Sun's small scale global photospheric magnetic field

Meyer, Karen A.
Mackay, D. H.

MODELING THE SUN'S SMALL-SCALE GLOBAL PHOTOSPHERIC MAGNETIC FIELD

K. A. Meyer[1] AND D. H. Mackay[2]
[1] Division of Computing and Mathematics, Abertay University, Kydd Building, Dundee, Bell Street, DD1 1HG, Scotland, UK; k.meyer@abertay.ac.uk
[2] School of Mathematics and Statistics, University of St Andrews, North Haugh, St Andrews, KY16 9SS, Scotland, UK

ABSTRACT

We present a new model for the Sun's global photospheric magnetic field during a deep minimum of activity, in which no active regions emerge. The emergence and subsequent evolution of small-scale magnetic features across the full solar surface is simulated, subject to the influence of a global supergranular flow pattern. Visually, the resulting simulated magnetograms reproduce the typical structure and scale observed in quiet Sun magnetograms. Quantitatively, the simulation quickly reaches a steady state, resulting in a mean field and flux distribution that are in good agreement with those determined from observations. A potential coronal magnetic field is extrapolated from the simulated full Sun magnetograms to consider the implications of such a quiet photospheric magnetic field on the corona and inner heliosphere. The bulk of the coronal magnetic field closes very low down, in short connections between small-scale features in the simulated magnetic network. Just 0.1% of the photospheric magnetic flux is found to be open at 2.5 $R_\odot$, around 10–100 times less than that determined for typical Helioseismic and Magnetic Imager synoptic map observations. If such conditions were to exist on the Sun, this would lead to a significantly weaker interplanetary magnetic field than is currently observed, and hence a much higher cosmic ray flux at Earth.

Key words: Sun: activity – Sun: corona – Sun: magnetic fields – Sun: photosphere

Supporting material: animations

1. INTRODUCTION

The Sun's magnetic activity varies from low to high across an approximately 11 year cycle. In addition to this, cycle amplitudes also vary from one cycle to the next (see, e.g., the review by Hathaway 2010 and references therein). In extreme cases, the Sun has been known to enter a grand minimum of magnetic activity, in which very few or no sunspots are observed. The most famous example of this is the Maunder Minimum, a seventy year period from 1645 to 1715 during which almost no sunspots were observed (Maunder 1890); although cyclic behavior was still present (Beer et al. 1998). Švanda et al. (2016) suggest that pores (white light photospheric features with strong magnetic fields) may have been invisible to observers at the time due to their lower resolution telescopes, but could potentially have contributed to the Sun's global dynamo and its continued reversal of its polar magnetic caps. The cause and lead up to this grand minimum is an interesting topic of study, for example Eddy et al. (1976) suggest that faster rotation at the equator and stronger overall differential rotation may have been linked to its onset. In the present paper, however, we are interested in the state of the solar photosphere once it has reached the deepest phase of a grand minimum of activity. One possibility is that only small-scale magnetic features were present during such a state. Indeed, Riley et al. (2015) suggest that in the later stages of the Maunder Minimum, the solar photosphere may have consisted entirely of small-scale ephemeral regions (ERs), with no significant large-scale magnetic dipole structure. Low solar magnetic activity results in less magnetic flux leaving the Sun (open flux) and hence a weaker interplanetary magnetic field (IMF), which in turn leads to a higher galactic cosmic ray intensity at Earth (see, e.g., Usoskin 2013 and references therein). In the current paper, we simulate an extremely low activity global photospheric magnetic field, in which no active regions or active region remnants are present. The properties and consequences of this low activity simulation are considered.

The Sun's photospheric magnetic field extends over a vast range of spatial and timescales; from the largest active regions, with physical extents of hundreds of megameters and lifespans of days to weeks (Harvey & Zwaan 1993), down to the smallest features of the inter-network, on the scale of a few hundred kilometers with lifespans of minutes to hours (de Wijn et al. 2008). The processes that determine the evolution of this magnetic field also cover a wide range of spatial and timescales, from the Sun's global differential rotation and meridional flow, which have timescales of 1/4 year and 2 years, respectively (Wang et al. 1989b; Mackay & Yeates 2012), down to the convective flows of granulation and supergranulation, with timescales of hours to days (Simon & Leighton 1964; Rieutord & Rincon 2010).

Many authors have studied the properties of magnetic features on the solar surface and the nature of their evolution. On the smallest scales (a few hundred to few thousand kilometers), authors such as Harvey (1993), Schrijver et al. (1997), Parnell (2002), Hagenaar et al. (2003), DeForest et al. (2007), de Wijn et al. (2008), Lamb et al. (2013), and Jin & Wang (2015) have considered the nature of the magnetic features of the so-called magnetic carpet. For studies on active region scales and global evolution see, for example, Harvey & Zwaan (1993), Parnell et al. (2009), and the references in Solanki (2003), Hathaway (2010), and van Driel-Gesztelyi & Green (2015).

In addition to observational studies, many models simulate the evolution of magnetic features across a variety of time and spatial scales. On the largest scales, Wang et al. (1989a) and Wang & Sheeley (1991) constructed a surface flux transport model that included differential rotation, meridional flow, and a supergranular diffusion term. Other authors considering the

large-scale evolution of solar and stellar photospheric magnetic fields based on flux transport models are, for example, Mackay et al. (2002a, 2002b), Mackay (2003), Schrijver & DeRosa (2003), Wang et al. (2005), Gibb et al. (2014), and Lemerle et al. (2015). For a review of flux transport models see Mackay & Yeates (2012). Recently, more sophisticated models have been developed, for example combining flux transport with the Babcock–Leighton dynamo model (Miesch & Dikpati 2014). The majority of the above models are macroscopic in nature, considering only the largest scales of magnetic features, where the random walk of smaller scale features within convective cells is approximated through a diffusion term. Several authors have constructed models for the evolution of small-scale magnetic features, building in a variety of the observed flux evolution processes including emergence, cancellation, coalescence, and fragmentation (e.g., Schrijver et al. 1997; Crouch et al. 2007), as well as the influence of underlying convective flows (e.g., Parnell 2001; Meyer et al. 2011).

Schrijver (2001) and Schrijver et al. (2002) modeled the global evolution of the Sun's photospheric magnetic field, incorporating magnetic features that spanned from active regions (few times 10^{22} Mx) down to ephermeral regions (few times 10^{19} Mx, e.g., Harvey 1993). They included differential rotation and meridional flow, but did not explicitly simulate supergranulation. Instead, magnetic features moved in random directions with a step length based upon their flux (greater flux resulting in smaller velocity) and a flux dispersal coefficient. The four flux evolution processes of emergence, cancellation, coalescence, and fragmentation were built into the model, although the emergence phase itself was not simulated —new magnetic features were inserted into the simulation under the assumption that the polarities had already separated. From the simulated photospheric magnetic fields, they considered the radiative losses of the Sun and other cool stars (Schrijver 2001), and the long-term evolution (several hundred years) of the photosphere (Schrijver et al. 2002).

Thibault et al. (2012, 2014) extended the magnetic carpet model of Crouch et al. (2007) to cover the full solar surface, and included active regions with properties determined from the cycle 21 sunspot database of Wang and Sheeley, as well as differential rotation and meridional flow. Emergence of new small-scale magnetic features was simulated by injecting individual mixed polarity magnetic elements at random spatial locations. Cancellation and coalescence were built into the model, but fragmentation was not explicitly included. They also did not include a supergranular flow profile, instead, similarly to Schrijver (2001), magnetic features moved in random directions with a specified step length. They simulated a full solar cycle, focusing in particular on the variation of their simulated magnetic network during this time.

The aim of this paper is to build on the magnetic carpet model of Meyer et al. (2011), extending the supergranular flow pattern and evolution processes to cover the full Sun. The eventual goal is to produce a global photospheric evolution model that includes the macroscopic active regions and global flows, as well as supergranulation and the microscopic flux evolution processes of the magnetic carpet. These processes, in particular supergranulation, play an important role in determining the random walk of magnetic flux across the solar surface as well as the fragmentation and redistribution of active region flux. For the present paper we focus first on the evolution of the small-scale magnetic field. Our study differs from those

discussed above as follows: (1) we define an actual supergranular flow profile, rather than approximating this as a random walk; (2) we explicitly simulate the emergence of new magnetic features by having opposite polarities move apart on appearance, with the probability distribution for newly emerging flux taken from the observational study of Thornton & Parnell (2011); and (3) the fragmentation of magnetic features is simulated, based on their flux and lifespan. The aim of the full model is to produce realistic surface simulations, as well as to provide a lower boundary condition to be coupled with a coronal field evolution model (e.g., Yeates et al. 2008).

The paper is structured as follows. The model is described in Section 2, including the construction of the global supergranular flow profile and a brief description for each of the four flux evolution processes. Results are presented in Section 3. We focus first on visual results, starting with the global photospheric magnetic field, then focusing on a smaller region to demonstrate the evolution of the model and how it compares to observed magnetograms. Next, quantitative results are presented for comparison with observed solar parameters. Finally, a global potential coronal magnetic field is extrapolated from one of the simulated global magnetograms. Its properties are compared with potential coronal fields extrapolated from active and quiet Sun synoptic maps observed by the Helioseismic and Magnetic Imager (HMI; Scherrer et al. 2012) on board the *Solar Dynamics Observatory* (*SDO*). Discussion, conclusions and future development of the model are given in Section 4.

2. MODEL

The full Sun photospheric model is a 2D surface model based on the Cartesian magnetic carpet model of Meyer et al. (2011), with calculations now in spherical coordinates and with a supergranular flow profile that is determined for the full Sun. At present, the supergranules in our model are not time-evolving. This is adequate for the present paper where we show the development of the surface magnetic field into a steady state, in which the rates of flux emergence and cancellation are equal. In addition, the small-scale features of the magnetic carpet tend to evolve on timescales of minutes to hours (e.g., de Wijn et al. 2008; Zhou et al. 2010; Lamb et al. 2013), whereas supergranule lifespans are on the order of one to several days (Hirzberger et al. 2008; Rieutord & Rincon 2010). Meyer et al. (2011) found that using non-time-evolving supergranules in the model did not produce unrealistic results. The parameters for the following model are the same as those used in the local model of Meyer et al. (2011). These were chosen based either on observational studies, or by varying and choosing the best fit when observations did not exist (e.g., Parnell 2001). Since the present study still considers local scale evolution and relatively short timescales, but now on a global scale, the existing parameters were deemed appropriate.

2.1. Magnetic Features versus Magnetic Elements

In order to avoid confusion in the following discussion, we define here what we mean henceforth by a *magnetic feature* as opposed to a *magnetic element*:

1. A magnetic feature is what is *observed* on the solar surface, as an irregularly shaped patch of magnetic flux (e.g., DeForest et al. 2007).

2. A magnetic element is a "block" of magnetic flux in our simulation that is given a Gaussian B_R profile when the simulated magnetogram is computed. As will be discussed in Section 3, several magnetic elements can compose an irregularly shaped magnetic feature.

The radial magnetic field, $B_{R,j}$, at a distance of r from the center of a magnetic element j is given by

$$B_{R,j} = B_{0,j} e^{-r^2/r_{0,j}^2}, \qquad (1)$$

where $B_{0,j}$ is the element's peak magnetic field strength and $r_{0,j}$ is its Gaussian half-width, both determined from its flux, ϕ_j (see Meyer et al. 2011 for further details). The contribution of all magnetic elements is summed to compute the full magnetogram:

$$B_R = \sum_{j=1}^{N} B_{R,j}. \qquad (2)$$

2.2. Supergranular Flow Profile

One of the key features of the model is the small-scale convective flow that dominates the evolution of the magnetic elements on the solar surface. We now describe how this is specified. Hirzberger et al. (2008) found supergranule areas to span from 160 to 2000 Mm^2, with a roughly log-normal distribution and a mean of 575 Mm^2. Assuming the supergranules to be approximately circular ($R = \sqrt{A/\pi}$), this gives radii spanning from $R_{\min} = 7.1$ Mm to $R_{\max} = 25.2$ Mm, with a mean of 13.5 Mm. We randomly generate enough supergranules to fill the full solar surface, with their radii fitting this log-normal distribution.

The horizontal flow profile within an individual supergranule is given by

$$v_R = A_0 R \exp\left\{ \frac{-R^2}{R_{\max}^2} \right\}, \qquad (3)$$

where A_0 is the parameter determining the physical extent of the supergranule, $R_{\min} \leqslant A_0 R_{\max} \leqslant R_{\max}$. The flow profile for the full Sun is produced by summing all of the individual flow profiles, after which we scale the flow profile so that the peak is 1 km s^{-1} and the mean flow is roughly 0.35 km s^{-1}. For the simulation discussed in Section 3, 7428 supergranules were generated to cover the full Sun. A stronger supergranule (with $A_0 = 2.0$), in which no emergence is allowed to occur, is placed at each of the poles, to prevent magnetic elements from crossing them. A randomly directed velocity representing the contribution of granulation is also included, across the full solar surface. This contribution will tend to be weaker at the center of a supergranule and stronger at the boundaries between supergranules: 0–0.1 km s^{-1} within 0.75 of the supergranule cell radius of its center, 0–0.2 km s^{-1} otherwise. This helps to prevent magnetic elements from becoming stationary once they reach the network between cells.

The velocities of magnetic elements are usually determined from the underlying convective flows. In addition to this, however, there are times, such as when the magnetic elements are undergoing emergence or cancellation, that their velocities are not dominated by supergranulation but specified in other ways. These processes will be described in the following sections.

2.3. Emergence

New magnetic flux appears on the solar surface via the process of flux emergence. As in Meyer et al. (2011), flux emergence within our model is determined by the probability distribution of Thornton & Parnell (2011):

$$N(\phi_{\text{bp}}) = \frac{n_0}{\psi_0} \left(\frac{\phi_{\text{bp}}}{\psi_0} \right)^{-\alpha}, \qquad (4)$$

where $n_0 = 1.77 \times 10^{-14}$ cm^{-2} day^{-1}, $\psi_0 = 10^{16}$ Mx, and $\alpha = 2.74$. Integrating Equation (4) over the range $[\phi_a, \phi_b]$ Mx gives the number of bipoles expected to emerge per cm^2 per day, with an absolute flux in that range. We compute the number of bipoles expected to emerge across the full Sun for the full simulation in discrete intervals of length $2\phi_0 = 8 \times 10^{16}$ Mx, where bipoles in the range $[\phi_a, \phi_b]$ are assigned a flux of $\phi_a + \phi_0$. The flux range for newly emerging bipoles in our simulation is 8×10^{16}–4×10^{20} Mx (with individual polarities having flux in the range 4×10^{16}–2×10^{20} Mx), and every magnetic element within the simulation must have flux that is an integer multiple of the unit flux, $\phi_0 = 4 \times 10^{16}$ Mx. This gives an emergence frequency of approximately 5.5×10^7 bipoles per day, or 640 bipoles per hour across the full Sun. Each bipole is assigned a random time step of emergence and supergranule to emerge within. The time step for the simulation is 1 minute and it is run for 3000 time steps (50 hr) in total.

Magnetic elements are treated as "points" within the simulation, with arrays containing their defining parameters (position, flux etc.) updated at each time step. A magnetogram can then be computed by assigning each element a Gaussian profile in B_R and summing over all of their Gaussian profiles (Equation (2)). When a bipole is inserted into the simulation, the points representing the two opposite polarity elements are co-located. These points initially move in opposite directions (determined by a randomly assigned tilt angle) until they reach a separation of $1.5d(\phi_{\text{bp}}/2)$, where $d(\phi_{\text{bp}}/2)$ is the diameter of each element (see Meyer et al. 2011 for further details). Their initial separation velocity is 5 km s^{-1}, slowing to 0.5 km s^{-1}, in line with observations of such small-scale elements (e.g., Harvey 1993; Hagenaar et al. 2003). Once the magnetic elements have reached the specified separation, their subsequent motion is determined entirely by the underlying supergranular flow profile until another process takes over (fragmentation, coalescence, cancellation). Since the opposite polarity elements overlap completely when first inserted, they do not contribute flux to the simulated magnetogram. As they move apart, the effect in the simulated magnetogram is that their B_R profiles grow in flux until they have separated completely, simulating the emergence of magnetic field as is observed. New magnetic elements can also be produced via the breaking apart of an existing magnetic element, described below.

2.4. Fragmentation

Fragmentation is the breaking apart of a magnetic element into two or more smaller elements. Within our model, the

fragmentation process is based upon that of Parnell (2001), where the probability of fragmentation depends on a magnetic element's flux and age. It is possible for any element of flux greater than $2\phi_0 = 8 \times 10^{16}$ Mx to fragment during any time step, however older and larger elements have a greater probability of fragmentation. Based on the recommendation of Parnell (2001), we choose a fragmentation rate of $R_f = 1.5 \times 10^{-4}$ s^{-1}. Within the simulation, for an element to undergo fragmentation, its flux ϕ must satisfy

$$\phi > \psi(1 - k_f/q), \tag{5}$$

where $\psi = 8 \times 10^{18}$ Mx, $k_f = 0.75$ and $k_f < q < 1$ is randomly generated for each element, every time step. To introduce a random time-dependence, an element satisfying Equation (5) will only undergo fragmentation if

$$s < T/T_f, \tag{6}$$

where $0 < s < 1$ is random, T is the age of the magnetic element and $T_f = 1/R_f$. It can be seen that the maximum value that the right-hand side of Equation (5) may take is 2×10^{18} Mx, and Equation (6) will always be satisfied once $T \geqslant T_f$. Therefore every element with flux greater than 2×10^{18} Mx will fragment within $T_f = 1/R_f \approx 1$ hr 50 minutes, but it is possible for smaller, younger elements to fragment as well.

At present, an element may only split into two new elements at a given time, but may go on to split several more times in succession. If Equations (5) and (6) are satisfied for an element of flux ϕ, it will split into two new elements of flux ϕ_1 and ϕ_2. A random number p is chosen such that $0.55 \leqslant p \leqslant 0.95$, then

$$\phi_1 = \text{round}\left(\frac{p\phi}{\phi_0}\right)\phi_0,$$

so that ϕ_1 is an integer multiple of unit flux ϕ_0, and $\phi_2 = \phi - \phi_1$.

The two new "child" elements will have the same speed as the "parent" element had before fragmentation, and direction of motion $\pm 0.3\pi q$ from their original direction, where $0 < q \leqslant 1$ is a random number.

The opposite process to fragmentation is coalescence, where like polarity magnetic elements merge together, or cancellation in the case of opposite polarity magnetic elements. These processes are described below.

2.5. Cancellation and Coalescence

Cancellation and coalescence are treated as the same process within the simulation, the only difference is whether the elements involved are of the same or opposite polarity. At present, an element may only cancel/coalesce with one other element at a time, but may subsequently cancel/coalesce with additional elements at later times. Two elements ϕ_1 and ϕ_2 are defined to be within their interaction range if the distance between their centers is less than $0.5(d(\phi_1) + d(\phi_2))$, where $d(\phi_1)$ and $d(\phi_2)$ are their respective diameters. If this is the case, the two elements will cancel/coalesce only if they satisfy additional conditions, namely:

1. To prevent pairs of emerging/fragmenting elements from immediately canceling/coalescing with their process partner, they cannot do so with that partner unless they have completed the process of emergence or fragmentation. The process is complete once the elements have

reached the specified separation distance discussed in the above sections.

2. Elements already undergoing cancellation/coalescence cannot begin the process with a new element until the current process is complete. The conditions for this are described below.

Once it has been determined that two elements will cancel/coalesce, they move toward one another with a constant velocity of 1 km s^{-1} until their centers meet. Once their centers meet, in the case of coalescence or partial cancellation, one of the elements will be removed and the other element will take on the sum or difference between their fluxes as appropriate. In the case of full cancellation, where the two elements have equal and opposite flux, both elements are removed from the simulation. Within the simulated magnetogram, coalescence is observed as two elements merging together to create a larger element as their B_R profiles overlap. In the case of cancellation, the elements' B_R profiles shrink as they overlap.

2.6. Parallelizing the Model

The model is required to handle the evolution of several millions of small-scale magnetic elements at a time. Due to this, we parallelized the model to increase its speed and efficiency. The simulation is parallelized so that each processor models a region of equal area, and hence a roughly equal number of magnetic elements. Processors are only required to communicate with nearest neighbors to check for cross-processor interaction of magnetic elements. This optimization is highly efficient.

As mentioned previously, elements are treated as "points" within the simulation, with arrays containing their defining parameters. Global magnetograms may be calculated at any time and at any desired resolution, but are not calculated at every time step so as not to slow the code. The calculation of global magnetograms from the data held within the simulation is parallelized, but is still relatively time-consuming. Therefore, global Sun magnetograms are only computed at specific time steps of interest. In addition to the global magnetograms, a local magnetogram times series can also be easily calculated for small sub-regions within the simulation.

3. RESULTS

Figure 1(a) shows a full disc image of the photospheric magnetic field produced by the simulation after $t = 49.7$ hr. At present, the simulation only produces the radial magnetic field, B_R. The full magnetogram has been wrapped around a sphere, and B_R has been multiplied by a cosine factor to produce a line of sight foreshortening effect. Figure 1(b) shows a planar map representation of the full Sun magnetogram at the same time, having "unwrapped" the sphere. The map is computed with 3600×1440 pixels, the same as an SDO/HMI line of sight synoptic map. This allows us to compare global potential magnetic fields computed from both the simulated planar maps and observed synoptic maps (see Section 3.1).[3]

We start the simulation from an empty Sun. As the simulation progresses, new magnetic elements emerge as bipoles within the supergranular cells and evolve based on

---

[3] Note that the simulated planar map is constructed from a single time frame, as opposed to latitudinal slices taken throughout solar rotation in the case of a synoptic map.
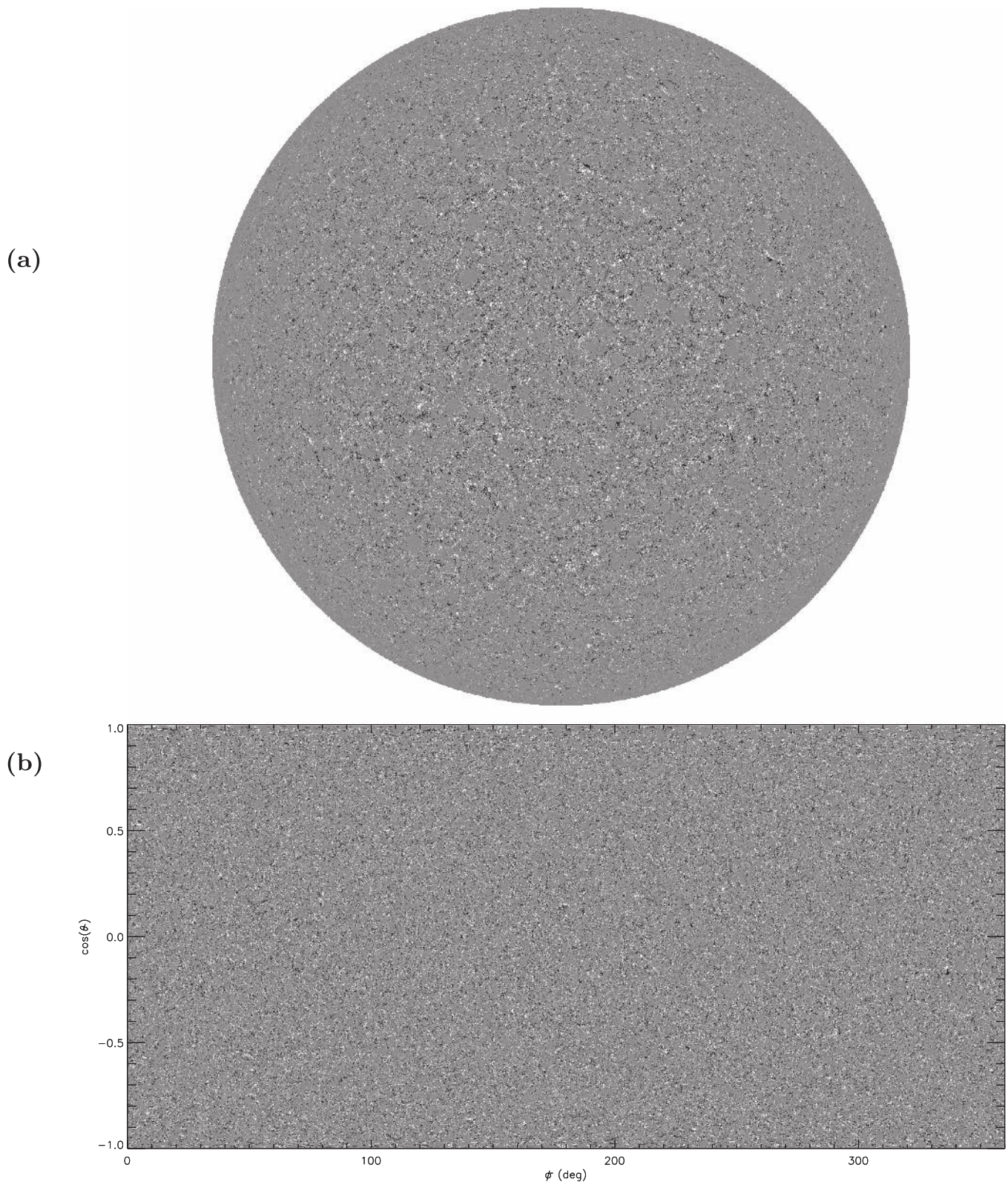
Figure 1. Photospheric magnetic field at $t = 49.7$ hr, viewed (a) on the solar disc (centered at $\phi = 0$, $\theta = 90$ deg) and (b) as a planar representation, both saturated at ± 30 G.

the underlying supergranular velocity profile as well as through interactions with one another. Figure 2 shows a planar map from the simulation after $t = 1$ hr. The four images below, (b) −(e), show enlarged snapshots of the region indicated by the white box in (a) at (b) $t = 1$ hr, (c) $t = 3.3$ hr, (d) $t = 10$ hr,

and (e) 45.3 hr. The region considered lies across the equator and is aproximately 278×278 Mm in size. These snapshots illustrate the time-evolving nature of the simulation and the filling of the region as the simulation progresses. Similar results are found for all other locations in the simulation. In (b) and (c),
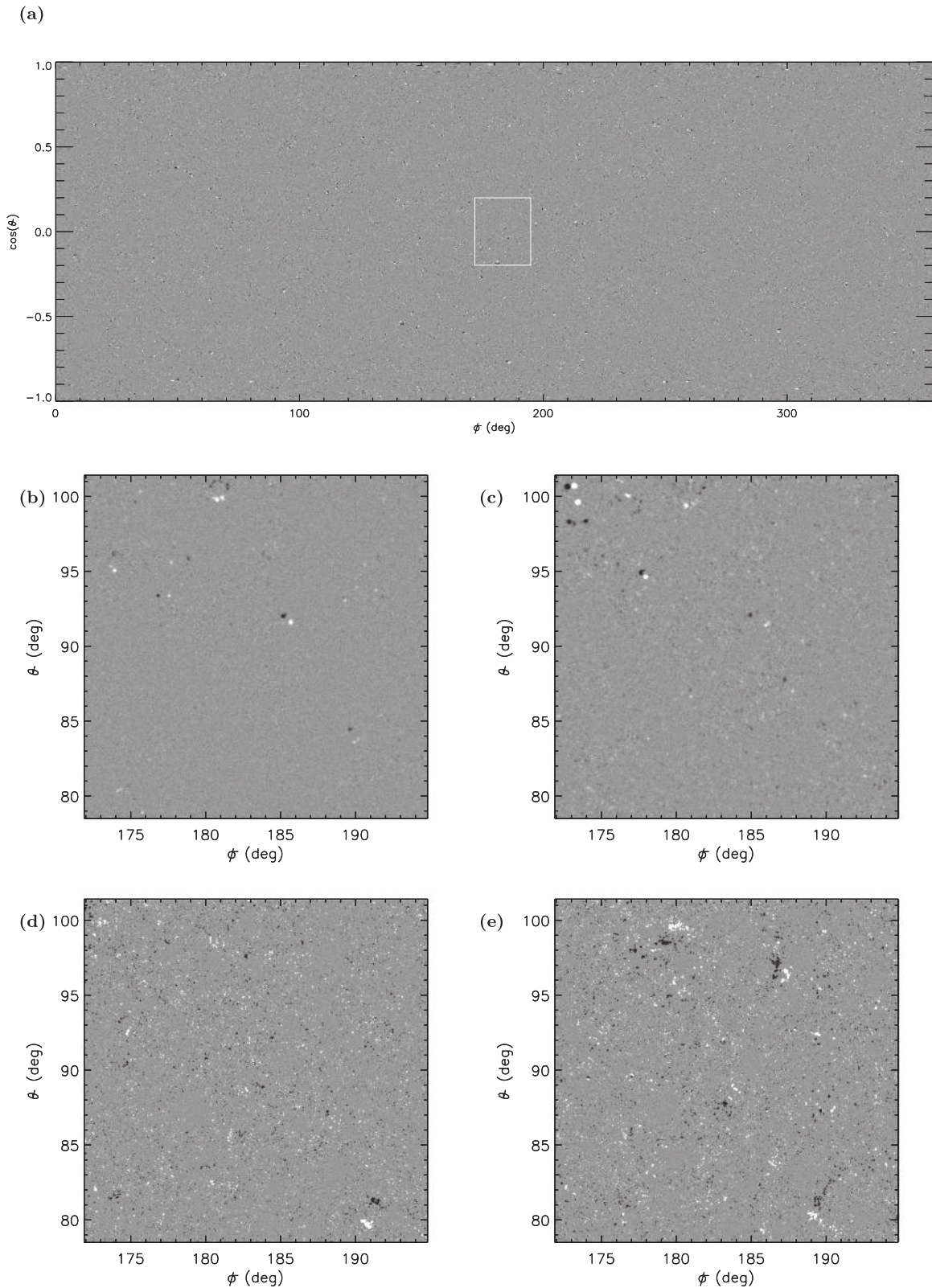
Figure 2. (a) Full Sun planar map at $t = 1$ hr, saturated at ± 30 G. (b)−(e) Zoomed in magnetogram region (indicated by white box on (a)) at (b) $t = 1$ hr, (c) $t = 3.3$ hr, (d) $t = 10$ hr and (e) 45.3 hr, saturated at ± 100 G.

near the start of the simulation, the magnetic elements appear largely circular due to their assigned Gaussian profiles. There are also only a small number of "larger" elements. By $t = 10$ hr in image (d), and even more so by $t = 45.3$ hr in (e), the magnetic elements appear much more irregularly shaped as "clumps" form composed of multiple overlapping Gaussian profiles, giving a more realistic effect. One can also see the outline of the underlying supergranular cell pattern as these
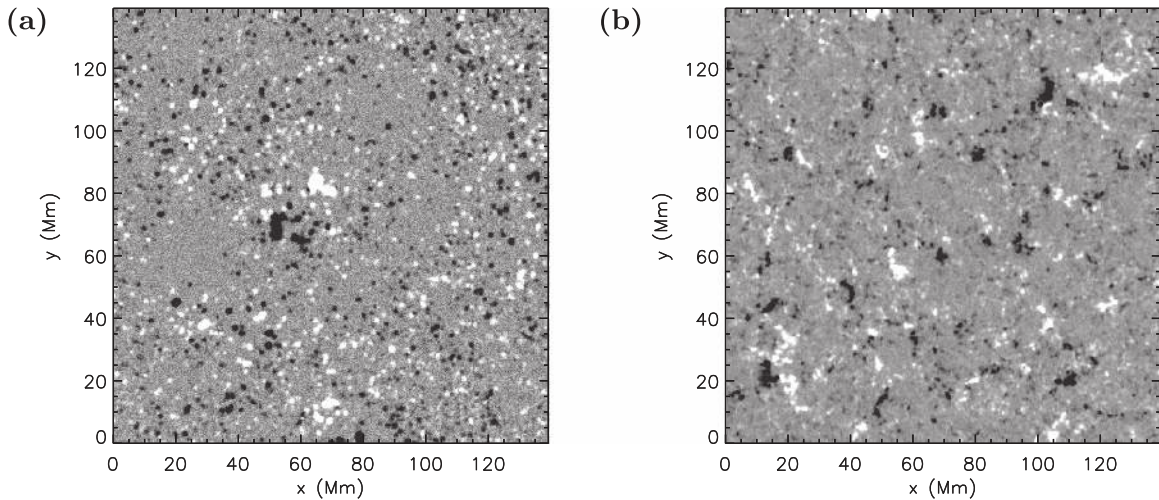
Figure 3. (a) Simulated magnetogram at $t = 27$ hr, centered at $\phi = 304$, $\theta = 74$ deg, with random noise in the range $\pm 2\sigma = 9.701$ G. (b) HMI magnetogram centered at $x = 1.64$, $y = -77.68$ arcsec, at 23:46:22 on 2011/01/18. All saturated at ± 30 G. Movies of (a) with and without noise are included (feb20fs_Mm.mpg and feb20fs_Mm_noise.mpg).

(Animations (a and b) of this figure are available.)

larger clumps form a magnetic network along the supergranule boundaries.

Figure 3 shows a direct comparison between (a) a region of a simulated magnetogram and (b) a quiet Sun region observed by HMI. The simulated magnetogram region is taken at $t = 27$ hr in the simulation and is an equatorial region of size 139×139 Mm (approximately 192×192 arcsec). The HMI magnetogram was observed close to disc center, and is of the same size and resolution (≈ 0.5 arcsec) as the simulated magnetogram. Both magnetograms are saturated at ± 30 G. The noise level in the HMI magnetogram was estimated to be $2\sigma = 9.701$ G by fitting a histogram to pixel values over a 24 hr series of HMI data which includes this image. Random noise in the range $\pm 2\sigma$ has also been added to the simulated magnetogram. The noise is added purely for a more realistic visual comparison, and is not included in any quantitative analysis. The simulated magnetogram clearly contains more rounded magnetic elements due to their Gaussian B_R profile, but larger, irregularly shaped features and a magnetic network have been produced on the same scale as observed in the HMI quiet Sun region. Movies showing a time series of the simulated region in (a) are included in the online journal, showing the region with and without the addition of random noise. Of particular interest in the movies is the emergence and subsequent fragmentation of a large bipole near the center of the region, forming the bipolar feature seen at the center of image (a).

Figure 4 provides quantitative information. Plot (a) shows the mean magnetic field as a function of time (black line) calculated directly from the simulation, where each magnetic element is treated as a "point." To compute this, the absolute fluxes of all magnetic elements are summed up and divided by the total area of the Sun to give an estimate of the mean magnetic field in the simulation. This will always be an upper estimate for the mean field, and in general will tend to over-estimate it. The red stars show the mean magnetic field computed directly from the simulated magnetograms. When the magnetogram is computed, many of the magnetic elements' Gaussian B_R profiles overlap. This is why the "true" mean magnetic field of the magnetogram is always slightly less than that calculated when treating the elements as points. It is also

likely that a small fraction of magnetic flux will be "lost" due to numerical error when computing the magnetogram, but this can be minimized by choosing a sufficiently high resolution. The importance of this intermediate calculation of the magnetic field from the simulated point elements is that it shows the general trend of the quantity without having to calculate computationally heavy full Sun magnetograms. For example, the plot here shows that there is an initial rapid increase in the mean field, followed by it beginning to level off and approach a steady state. This gives us an indication of the simulation's behavior to inform our choice of times of interest in which we may wish to compute full or sub-region magnetograms.

For the full Sun magnetograms used to compute the mean field values (red stars) in Figure 4(a), the resolution was chosen to be the same as a high-resolution HMI magnetogram (≈ 0.5 arcsec), both to minimize flux loss and for a direct comparison with observed magnetograms. This results in a 11962×5981 pixel magnetogram which is computationally expensive to compute, therefore full Sun magnetograms have only been produced at selected times. Although the red stars are consistently lower than the black line, they follow the same trend. The value of 7–8 G for this steady state is in line with observations of the quiet Sun mean field. The box in the lower right of the plot shows a zoomed section of the last 7 hr of the simulation. It can be seen that the mean field is still gradually increasing at this stage, at a rate of around 1.7×10^{-4} G per minute. The study of Meyer et al. (2011), which used the same simulation parameters, suggests that this should level off if left for longer (simulations in Meyer et al. 2011 were run for 250 hr in total). For the present study, however, 50 hr is the limit to which we believe it is reasonable to run the full Sun simulation without beginning to consider larger-scale evolution processes such as differential rotation and meridional circulation. These will be built in as part of a future study.

The simulation reaches a steady state when the rates of emergence and cancellation are equal. Figure 4(b) shows the emergence rate minus the cancellation rate (Mx cm^{-2} s^{-1}) for the full 50 hr simulation. The emergence rate is approximately steady for all time, as newly emerging bipoles determined from Equation (4) are randomly distributed throughout the simulation.
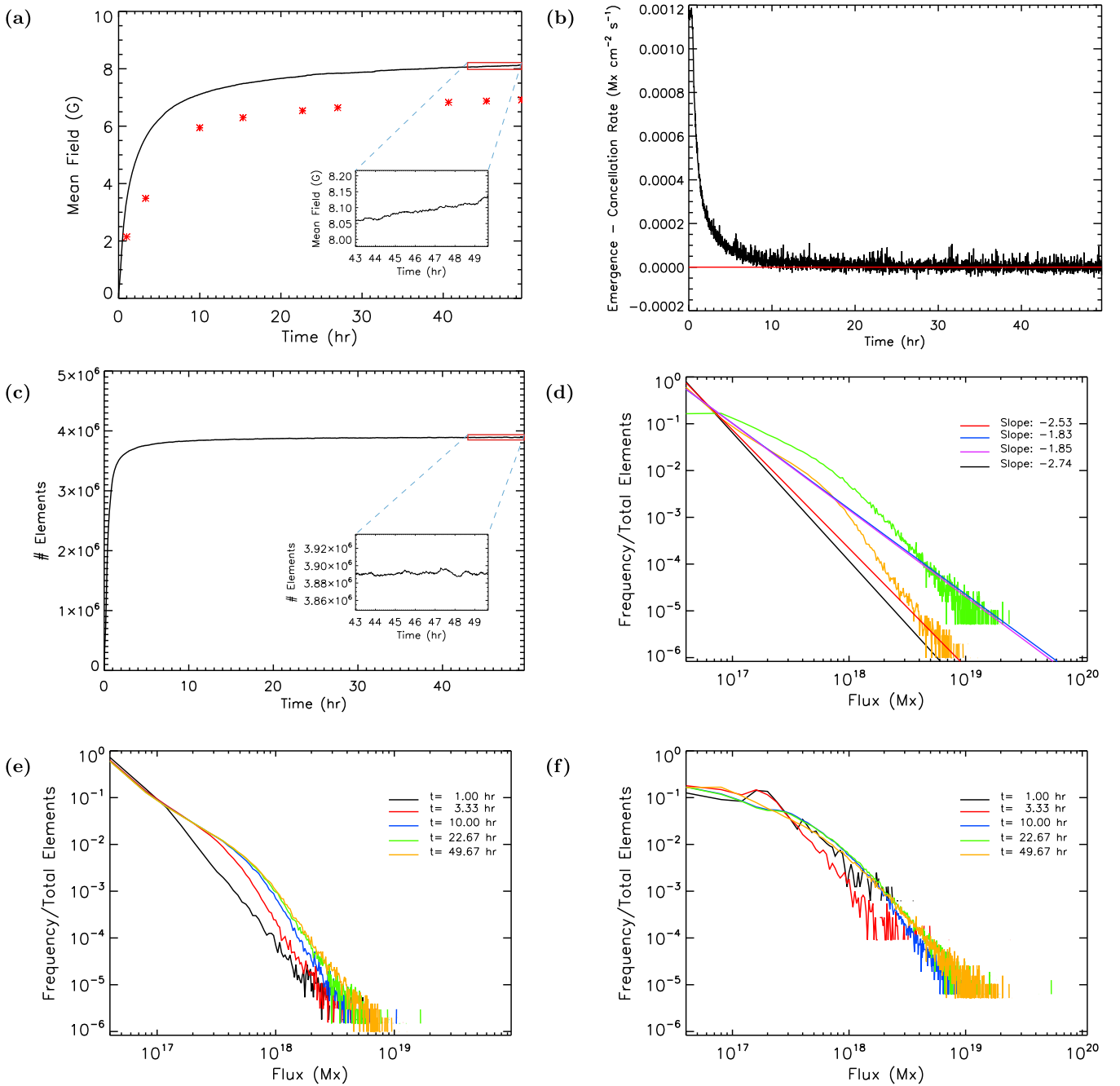
Figure 4. (a) Mean magnetic field as a function of time calculated from the simulation (magnetic elements, black line) and simulated magnetograms (red stars). (b) Emergence minus cancellation rate as a function of time for the simulation. (c) Number of magnetic elements in simulation as a function of time. (d) Flux distribution as calculated from the simulated magnetic elements (orange) and using the SWAMIS code to detect magnetic features in the simulated magnetograms (green). The purple line shows the observed power law determined by Parnell et al. (2009), the red line shows the power law fit to the magnetic element distribution (orange data) and the blue line shows the fit to the SWAMIS detected magnetic feature distribution (green data). The black line shows the slope of the observed emergence distribution that is built into the model (Thornton & Parnell 2011). (e) Flux distribution as calculated from the simulated magnetic elements, and (f) using the SWAMIS code to detect magnetic features in the simulated magnetograms, for a series of different times.

The cancellation rate rapidly increases from zero at the start of the simulation until it also becomes approximately steady after the first few hours. The result is that the emergence minus cancellation curve shows an initial rapid decrease, then oscillates about zero (red dashed line) for the remainder of the simulation. Due to this, we are satisfied that the simulation has reached a steady state.

Figure 4(c) shows the total number of magnetic elements in the simulation as a function of time. The curve levels off even more rapidly than the mean field or emergence minus cancellation rate. The mean magnetic field continues to increase after the number of magnetic elements has levelled off due to the formation of larger (greater flux) magnetic elements through coalescence, forming the magnetic network. The total number of magnetic elements levels off around 3.8×10^6, which is greater than that expected from observations of the Sun at any instant. The box in the lower right of the plot shows a zoomed section for the last 7 hr of the simulation. The average change in the number of elements at this
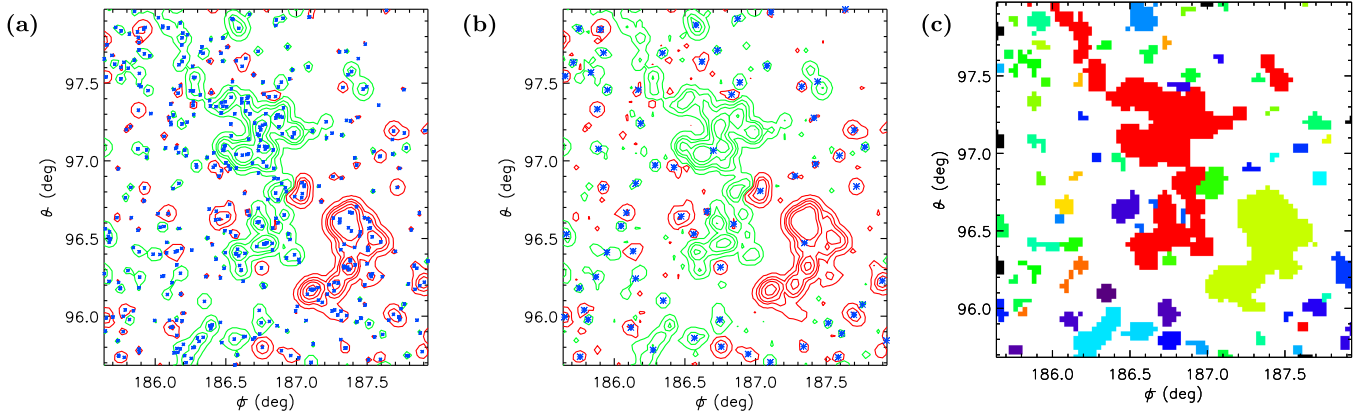
Figure 5. (a) Simulated magnetogram at $t = 49.7$ hr, centered at $\phi = 187$, $\theta = 97$ deg. Contours of magnetic field (red = positive, green = negative) are displayed at $\pm[10, 50, 100, 200, 350]$ G. Blue stars indicated the locations of the centers of all individual Gaussian magnetic elements in the region. (b) As in (a), but blue stars now represent the centroids of all magnetic features detected by SWAMIS in the region. (c) Same region, with different magnetic features identified by SWAMIS in different colors.

Table 1
Table of Values for Magnetic Elements within The Simulation, and Magnetic Features Identified by SWAMIS within The Simulated Magnetogram

	Simulation Values (Magnetic Elements)	SWAMIS Values (Magnetic Features)	Predicted (Equation (7))
No. of features	1,012,294	192,534	207,000
Min. feature flux	4×10^{16} Mx	4.004×10^{16} Mx	…
Max. feature flux	2.888×10^{19} Mx	1.105×10^{20} Mx	…
Mean feature flux	1.262×10^{17} Mx	4.436×10^{17} Mx	5.1×10^{17} Mx
Total feature flux	1.278×10^{23} Mx	8.541×10^{22} Mx	…
Mean field	8.04 G	6.9 G (magnetogram)	6.6 G

Note. Values computed from magnetogram region $(\phi, \theta) \in [0, 360] \times [75, 105]$ deg at $t = 49.7$ hr.

time is just 2 per minute. Parnell et al. (2009) determined a power law relationship between the frequency of solar magnetic features versus feature flux. The form used in Meyer et al. (2011) to determine the expected number of observed magnetic features is:

$$M(\phi) = \frac{N_f}{\psi_0}\left(\frac{\phi}{\psi_0}\right)^{-1.85} \text{cm}^{-2}, \qquad (7)$$

where $N_f = 3.6 \times 10^{-17} \text{cm}^{-2}$ and $\psi_0 = 10^{16}$ Mx. Integrating Equation (7) over the range of element fluxes in our simulation indicates that over an order of magnitude more elements are found in the simulation than would be expected in reality. The observed law (Equation (7)) suggests that there should be just 790,000 features with fluxes in the range 4×10^{16}–10^{20} Mx. This discrepancy is due to our differing definitions of a magnetic "feature" or "element"; one "feature" as identified by Parnell et al. (2009) may be composed of many tens of overlapping Gaussian elements in our simulation. This is illustrated by Figure 5(a), which shows a zoomed in region of the simulated magnetogram at $t = 49.7$ hr, with contours of magnetic field in red (positive) and green (negative). Blue stars overplotted indicate the centers of all the individual Gaussian magnetic peaks. To resolve this issue, we used the same feature tracking code as was used to obtain the power law of Parnell et al. (2009) to identify features within our simulated magnetograms.

The code used is called SWAMIS (DeForest et al. 2007; Lamb et al. 2013) with a "clumping" feature identification scheme, as applied by Parnell et al. (2009). The clumping feature scheme is chosen over other feature detection methods tested as they found it to be more robust when comparing data from different instruments and resolutions, as well as less sensitive to changes in sensitivity. Clumping identifies all connected, same-sign pixels above a certain threshold as a single feature. We set the minimum feature size to be 3 pixels, and the minimum pixel value for detection to 10 G. The input for the code was an equatorial region of the simulated magnetogram at $t = 49.7$ hr, spanning the full circumference of the equator and $15°$ in latitude either side, giving a region of approximately 4373×363 Mm. As discussed in Section 2.1, we will use the term "magnetic feature" to describe a feature identified by SWAMIS, and "magnetic element" to describe the individual "points" whose properties are held in arrays within our simulation. Figure 5(b) shows the same magnetogram region as Figure 5(a), but now the blue stars indicate the centroids of all of the magnetic features detected by SWAMIS. Comparing with (a), it can clearly be seen that significantly fewer features are detected by SWAMIS than there are individual elements within the simulation. For illustrative purposes, Figure 5(c) shows the same region again, with different features detected by SWAMIS displayed in different colors.

A summary of quantitative results from SWAMIS is given in Table 1 alongside results determined "directly" from individual elements in the simulated region. Predicted values for the mean

flux (ϕ_{avg}) and mean field (B_{avg}) are calculated from Equation (7) as follows (Meyer et al. 2011):

$$B_{\mathrm{avg}} = \int_{\phi_{\mathrm{min}}}^{\phi_{\mathrm{max}}} M(\phi)\phi \, d\phi = \frac{N_f \psi_0}{0.15}\left[\left(\frac{\phi}{\psi_0}\right)^{0.15}\right]_{\phi_{\mathrm{min}}}^{\phi_{\mathrm{max}}} \quad (8)$$

and

$$\phi_{\mathrm{avg}} = \frac{B_{\mathrm{avg}}}{N_{\mathrm{tot}}}, \quad (9)$$

where

$$N_{\mathrm{tot}} = \int_{\phi_{\mathrm{min}}}^{\phi_{\mathrm{max}}} M(\phi) \, d\phi = -\frac{N_f \psi_0}{0.85}\left[\left(\frac{\phi}{\psi_0}\right)^{-0.85}\right]_{\phi_{\mathrm{min}}}^{\phi_{\mathrm{max}}}.$$

SWAMIS detects an order of magnitude fewer magnetic features in the region than there are magnetic elements, which is in good agreement with the number of features predicted by Equation (7). The minimum size of feature detected is the same as the minimum element size, but the mean and maximum size of features detected by SWAMIS are several times larger, as expected. The mean feature size of 4.4×10^{17} Mx detected by SWAMIS is in good agreement with the mean feature size of 5.1×10^{17} Mx predicted by Equation (9). A mean magnetic field of 6.9 G is calculated from the synthetic magnetogram to which SWAMIS was applied. This is slightly lower than the mean field of 8.04 G calculated by summing the fluxes of all individual magnetic elements and dividing by the area of the magnetogram, for the same reasons as given when discussing Figure 4(a): due to magnetic elements' Gaussian profiles overlapping when computing the magnetogram. The mean field of the synthetic magnetogram is also in good agreement with the mean field predicted by Equation (8).

The orange curve in Figure 4(d) shows the flux distribution calculated directly from the simulation, where magnetic elements are binned according to their simulation flux value. The red curve overplotted is a power law fit to this data. The green curve shows the flux distribution as determined from the simulated magnetograms using SWAMIS, where magnetic features are detected as "clumps" that may be composed of many individual magnetic elements. The blue curve overplotted is a power law fit to the SWAMIS data. For comparison with the two power law fits discussed above (red and blue), the observed power law determined by Parnell et al. (2009) is overplotted in purple, and the power law for newly emerging flux (Equation (4)) is plotted in black. The fit to the simulated magnetic elements distribution (red) is much closer to the line of the emergence distribution (black), with slopes of −2.53 and −2.74, respectively. The magnetic element slope (red) is slightly shallower than the emergence slope (black), due to larger elements forming than emerge, but is still much steeper than that of Parnell et al. (2009) (purple). As discussed above, this is unsurprising due to our differing definitions between magnetic features and magnetic elements, and the true comparison should be with the SWAMIS detected slope. The fit of the SWAMIS detected flux distribution (blue) is excellent when compared with the Parnell et al. (2009) power law (purple), with slopes of −1.83 and −1.85, respectively. This demonstrates the success of our model in reproducing the behavior of small-scale photospheric magnetic features, as a

consequence of the emergence and evolution of smaller magnetic elements. For interest, a time series of histograms is shown for both the simulated magnetic elements (e) and the SWAMIS detected magnetic features (f). In both cases, the histograms tend to move toward the right as larger magnetic elements or features form, but the slopes of the SWAMIS histograms are consistently less steep due to the greater number of large, complex features formed in the simulated magnetograms. A future study will compare series of simulated and HMI small-scale magnetograms using SWAMIS, so that aspects of the simulated flux evolution processes (e.g., timescales, velocities) may be quantitatively compared with observations to determine their realism, and the model modified as appropriate.

3.1. Coronal Magnetic Field

In the present study, we do not consider the coronal magnetic field in any great detail. Here we consider potential field extrapolations purely for visual comparison and to speculate on the coronal structure of a grand minimum state Sun, as potential field source surface (PFSS) extrapolations are widely used by the scientific community. For a more in-depth study of grand minimum coronae, Riley et al. (2015) compare the magnetic structure and emission of coronae for various hypothetical grand minimum photospheric states using a thermodynamic MHD model.

A potential magnetic field was extrapolated from a simulated full Sun magnetogram at $t = 49.7$ hr for comparison with potential fields extrapolated from quiet (CR2097, 2010 May) and active (CR2142, 2013 September) *SDO*/HMI synoptic maps. To create an equivalent lower boundary condition from the simulated magnetogram, it was interpolated to a planar map of the same resolution as an HMI synoptic map: 3600×1440 in longitude and cosine colatitude. Considering first the photospheric magnetic field of each map, Figure 6(a) shows the absolute flux through the photosphere as a function of colatitude, for the simulation (black), CR2097 (red), and CR2142 (blue). There are clear spikes in the absolute flux at active latitudes in the active case, CR2142, and to a lesser extent in CR2097 due to weaker and decayed active regions. The absolute flux of the simulation displays a sinusoidal profile with colatitude, since magnetic features are evenly distributed across the solar surface. From this it is clear that even during solar minimum, decaying or remnant active region flux plays a role at low latitudes. There is a clear overlap in the absolute flux of the simulation and of the quiet Sun synoptic map CR2097 for around 40° across the solar equator, indicating that the simulation has correctly described the photospheric magnetic field strength in this region. Around the poles, however, the flux of the two HMI maps is much higher than that of the simulation. This is due to meriodional circulation transporting remnants of decaying active regions poleward to form near-unipolar caps, achieving peak strength around solar minimum (e.g., Babcock 1959). With no active regions emerging (and indeed no meridional circulation at present), a build-up of magnetic flux at the poles does not occur in the simulation. From this it can be seen that there are clear differences between our quiet Sun model and a so-called quiet (low activity) observation of the Sun.

A potential field was extrapolated out to a source surface (R_{ss}) at 2.5 solar radii ($R_\odot$), from the simulation and HMI maps. Figure 7 shows field line plots for each of the potential fields, to give an
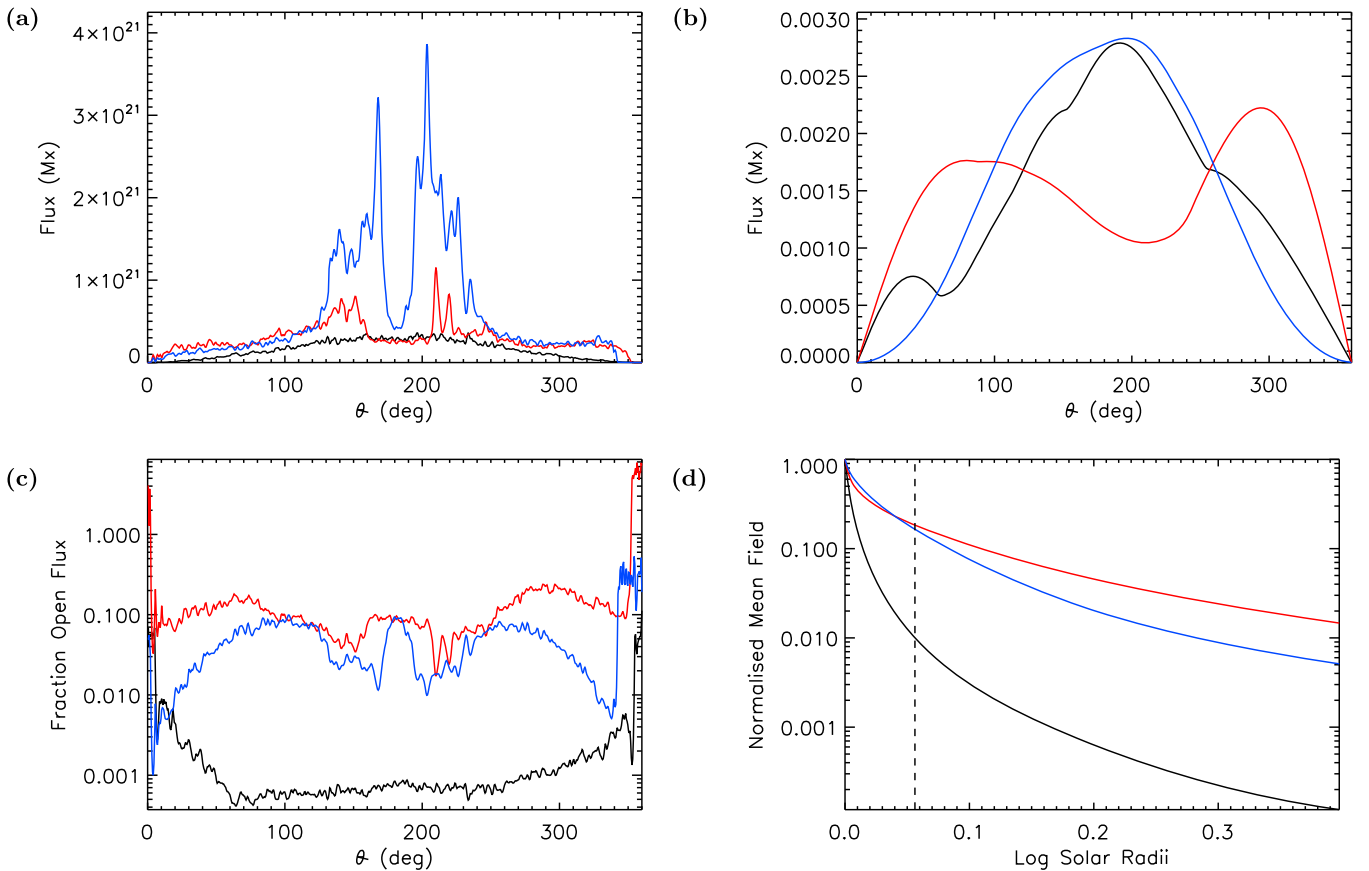
Figure 6. In each plot, line colors represent the simulation at $t = 49.7$ hr (black), HMI Carrington Rotation 2097 (red) and HMI Carrington Rotation 2142 (blue). (a) Absolute magnetic flux through photosphere vs. colatitude. (b) Normalized open flux vs. colatitude. (c) Fraction of open flux vs. colatitude. (d) Normalized mean field vs. solar radii. Vertical dashed line indicates where simulation mean field drops below 1% of its photospheric value.

impression of the overall coronal structure. In each case, field lines are plotted from starting points in the plane of sky at 1.25 $R_\odot$ and 1.5 $R_\odot$, at intervals of 10°. Note that for the simulation, this image is not representative of the bulk of magnetic connections, which close very low down (see, e.g., Figure 6(b) and the discussion below). Although the simulation represents a globally quiet photospheric magnetic field, its coronal field is very different to that of CR2097 which is an observation of the Sun during solar minimum in 2010. There is very little open field originating from the simulated magnetogram, whereas the potential coronal field of CR2097 has a clear dipolar structure, due to the aforementioned build-up of near-unipolar flux at the poles.

The overall coronal structure of the simulated magnetogram looks more similar to that of the active Sun observation, CR2142, however their photospheric magnetic fields are clearly vastly different. There are fewer open field regions in CR2142 than CR2097 due to most of the flux connecting between large active regions. In the case of the simulation, most of the flux closes down even lower in short connections between very evenly distributed small positive and negative magnetic features located in the magnetic network. Figure 6(b) shows the normalized flux through the source surface at 2.5 $R_\odot$, colored as in (a). As seen in Figure 7, the general structure of the open flux of the simulation (black) looks more similar to that of the active Sun corona (blue) than the quiet Sun corona (red). In the quiet case, CR2097, there are clear peaks toward the poles illustrating the Sun's dipolar structure at this stage of its activity cycle. The flux of the simulation and active Sun, CR2142, has an approximately sinusoidal distribution with

colatitude because the open flux is evenly distributed, there are no predominantly open regions. As mentioned above, however, the bulk of magnetic connections close very low down in the simulation, so there is very little open flux at all. Figure 6(c) indicates the fraction of open flux versus colatitude for each simulation. The plot was created by assuming that all of the open flux is purely radial from the photosphere to 2.5 $R_\odot$, hence was calculated simply as the ratio of the total flux at 2.5 $R_\odot$ to that at the photosphere at each colatitude. In reality, even a potential coronal field is much more complex than this assumption, but it is useful for illustrative purposes. The plot shows that for the mixed polarity, small-scale simulation, only around 0.1% of the flux is open, whereas for the two HMI synoptic maps, between 1% and 10% of the flux is open. Sharp increases in the open flux ratio near the poles are due to the potential field being space filling. There is very little surface flux in the polar regions of the HMI synoptic maps due to difficulty in observing the poles, and we have prevented magnetic elements from emerging or moving directly across the poles in our simulation (see Section 2). The extrapolated potential field expands into the polar regions, however, giving a higher value to this approximate ratio.

Table 2 shows the mean field at the photosphere and 2.5 $R_\odot$ for each of the potential fields, as well as the mean field at 2.5 $R_\odot$ as a percentage of photospheric mean field.[4] This is also

---

[4] Note: Mean field at the photosphere for the simulation is weaker in Table 2 than the value given in Table 1 due to significant reduction in magnetogram resolution, as well as smoothing during potential field extrapolation.
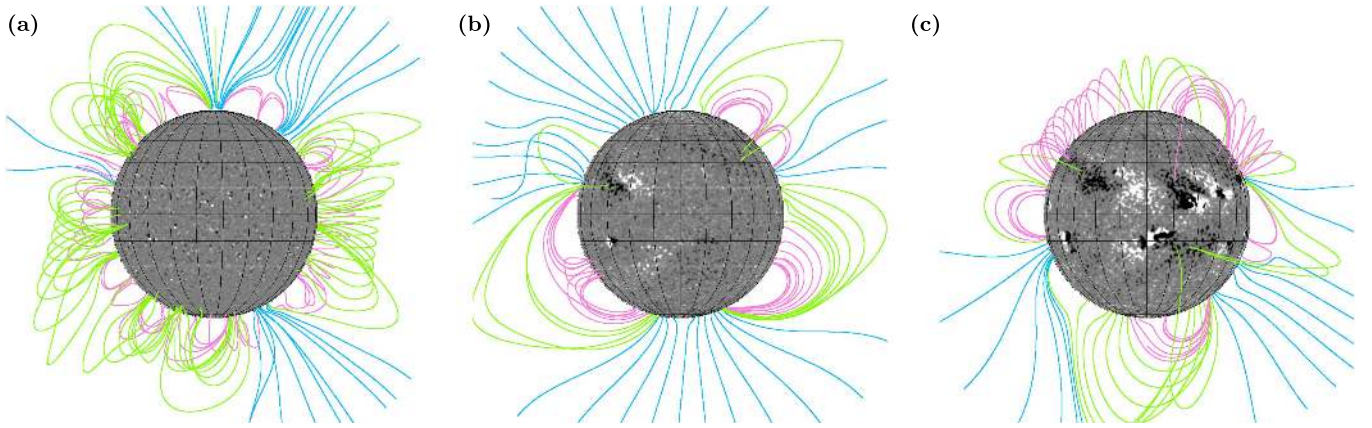
Figure 7. Potential field extrapolations from synoptic maps of (a) the simulation at $t = 49.7$ hr, (b) HMI Carrington Rotation 2097 (CR2097), and (c) HMI Carrington Rotation 2142 (CR2097).

Table 2
Mean Magnetic Field at The Photosphere and at 2.5 $R_\odot$ for Each of The Potential Fields Extrapolated

	Simulated Magnetogram	CR2097 (Quiet)	CR2142 (Active)
Mean field at photosphere	1.8 G	3.4 G	7.0 G
Mean field at 2.5 $R_\odot$	0.0002 G	0.05 G	0.04 G
% open flux	0.01	1.5	0.5

illustrated by Figure 6(d), which shows normalized mean field versus solar radii (black = simulation potential field, red = CR2097, blue = CR2142). The photospheric mean fields of the HMI magnetograms are higher than that of the simulation due to the presence of active regions and active region remnants. The mean field of the simulation planar map also drops off much more rapidly with height than either of the HMI synoptic maps. By 1.14 $R_\odot$ (indicated by vertical dashed line), the simulated magnetogram's mean field has decreased to less than 1% of its photospheric value, i.e., more than 99% of magnetic connections close down below this height. In contrast, the mean fields of CR2097 and CR2142 are at 18% and 17% of their photospheric values at this height. The complete absence of active regions or their remnants, as in the simulation, is one possibility for how the solar photosphere would look during a grand minimum of solar activity. If this were the case, with the coronal field behaving as illustrated by Figures 7(a) and 6(d), this would significantly reduce the strength of the IMF at Earth (1 au). From Table 2, the value of the mean field at 2.5 $R_\odot$ in the simulation is 0.0002 G. This would give a mean field at 1 au of just 2.9×10^{-8} G ($\approx 0.0002 R_{ss}^2/R_{1\,au}^2$). This is around 1000 times smaller than the typical values observed this century (≈ 3 nT $= 3 \times 10^{-5}$ G, e.g., Yeates et al. 2010), but it is also an order of magnitude lower than the ephemeral-only Sun estimates of Riley et al. (2015) (2.9×10^{-6} G for ± 10 G ERs, 8×10^{-7} G for ± 3 G ERs). Lee et al. (2011) suggest that the source surface for a PFSS should be lower during low solar activity (although interestingly, Réville et al. (2015) find the opposite). PFSS extrapolations were produced for the same simulated photospheric magnetic field as Figure 7(a) with different source surface heights, and the mean field at 1 au estimated for each of these. The results are summarized in Table 3. From the table, it is interesting to note that a factor of 6 decrease in the source surface height (2.5 $R_\odot$ to 1.25 $R_\odot$) produces a factor of 20

increase in the IMF at 1 au. The lower source surface extrapolations do produce IMF values closer to those of Riley et al. (2015) (around 100 times smaller than presently measured), but it should be noted that a PFSS is an very simplified and limited approximation to the coronal magnetic field. On further development of the global photospheric evolution model, we will consider a more realistic non-potential, time-evolving coronal magnetic field, for more detailed future studies.

4. DISCUSSION, CONCLUSIONS, AND FUTURE WORK

The aim of this paper was to construct a realistic model for the evolution of small-scale magnetic features across the full Sun, and consider the implications of such a quiet Sun for the corona and IMF. The model incorporates supergranulation and the flux evolution processes of emergence, cancellation, coalescence, and fragmentation. The simulation and magnetogram calculation codes are parallelized for efficiency, since several million small-scale magnetic features exist across the solar surface during any instant.

Qualitatively, the magnetic feature and network scales produced in the simulated magnetograms compare very favorably with observed *SDO*/HMI quiet Sun magnetograms. The simulation rapidly reaches a steady state, where the rates of emergence and cancellation are approximately equal, and the mean field produced is within the expected range for the quiet Sun. Using the SWAMIS feature identification code to compare the simulation with the results of Parnell et al. (2009), we find excellent agreement in the number of magnetic features produced, mean magnetic field and flux distribution slope.

A potential coronal field was extrapolated from a full Sun magnetogram late in the simulation, for comparison with potential fields extrapolated from HMI synoptic maps observed during solar maximum and solar minimum. The visual structure of the simulation coronal field is very different to that found in either of the HMI coronal fields. The mean field also drops off much more rapidly in height for the simulation, indicating that most connections close very low down. This is due to the lack of any active regions or active region remnants producing large, unipolar areas within the simulation. If this were representative of the Sun during a grand minimum of activity, it would have significant implications for the Earth. Such a rapid decrease in height of the Sun's coronal magnetic

Table 3
Mean Magnetic Field at 1 au for different Source Surface Heights

Source Surface Height	$1.25\ R_\odot$	$1.5\ R_\odot$	$2.0\ R_\odot$	$2.5\ R_\odot$
Mean field at 1 au	5.9×10^{-7} G	3.0×10^{-7} G	2.0×10^{-7} G	2.9×10^{-8} G

field would result in a very weak IMF, and hence greater exposure of the Earth to cosmic rays. Cosmic ray intensity at 1 au is known to be inversely correlated with solar activity (Usoskin et al. 1998, 2001). A much reduced level of magnetic activity and IMF would therefore result in a significant increase in cosmic rays at Earth. It has been suggested that there is a connection between cosmic rays and the Earth's climate, although the exact link is still an open question (see, e.g., Nesme-Ribes et al. 1993; Svensmark & Friis-Christensen 1997; Jørgensen & Hansen 2000; Usoskin & Kovaltsov 2008; Mironova et al. 2015).

In future, we plan to extend the full Sun model to incorporate active region scale magnetic features and their interaction with magnetic carpet scale features. As part of this, it will be required to introduce time-evolving supergranular flows as well as the processes of differential rotation and meridional circulation. One effect of time-evolving supergranules will be to help break apart magnetic elements, for faster convergence of the simulation to a steady state. For the present study, differential rotation and meridional circulation would not have had a significant net effect on the simulation due to the short timescale considered and because we have included no systematic orientation for the emergence of ERs. They will be vital to the realistic evolution of active regions, however, which can have lifespans of many weeks and tend to follow Joy's orientation law and Hale's polarity law. These large-scale flows will also have a significant effect on a time-evolving non-potential coronal magnetic field, which we intend to consider in future. It may also be of interest to consider the effect of a large-scale background magnetic field (dipole or quadrupole for example) on the small-scale magnetic network. In addition, it is our intention to further investigate smaller time- and spatial-scale simulated magnetograms, using SWAMIS to compare flux evolution processes within our model directly to those in observations. This will allow us to determine and improve their realism within the small-scale and global models.

REFERENCES

Babcock, H. D. 1959, ApJ, 130, 364
Beer, J., Tobias, S., & Weiss, N. 1998, SoPh, 181, 237
Crouch, A. D., Charbonneau, P., & Thibault, K. 2007, ApJ, 662, 715
de Wijn, A. G., Lites, B. W., Berger, T. E., et al. 2008, ApJ, 684, 1469
DeForest, C. E., Hagenaar, H. J., Lamb, D. A., Parnell, C. E., & Welsch, B. T. 2007, ApJ, 666, 576
Eddy, J. A., Gilman, P. A., & Trotter, D. E. 1976, SoPh, 46, 3
Gibb, G. P. S., Jardine, M. M., & Mackay, D. H. 2014, MNRAS, 443, 3251
Hagenaar, H. J., Schrijver, C. J., & Title, A. M. 2003, ApJ, 584, 1107
Harvey, K. L. 1993, PhD thesis, Utrecht Univ.
Harvey, K. L., & Zwaan, C. 1993, SoPh, 148, 85
Hathaway, D. H. 2010, LRSP, 7, 1
Hirzberger, J., Gizon, L., Solanki, S. K., & Duvall, T. L. 2008, SoPh, 251, 417
Jin, C., & Wang, J. 2015, ApJ, 806, 174
Jørgensen, T. S., & Hansen, A. W. 2000, JASTP, 62, 73
Lamb, D. A., Howard, T. A., DeForest, C. E., Parnell, C. E., & Welsch, B. T. 2013, ApJ, 774, 127
Lee, C. O., Luhmann, J. G., Hoeksema, J. T., et al. 2011, SoPh, 269, 367
Lemerle, A., Charbonneau, P., & Carignan-Dugas, A. 2015, ApJ, 810, 78
Mackay, D. H. 2003, SoPh, 213, 173
Mackay, D. H., Priest, E. R., & Lockwood, M. 2002a, SoPh, 207, 291
Mackay, D. H., Priest, E. R., & Lockwood, M. 2002b, SoPh, 209, 287
Mackay, D. H., & Yeates, A. R. 2012, LRSP, 9, 6
Maunder, E. W. 1890, MNRAS, 50, 251
Meyer, K. A., Mackay, D. H., van Ballegooijen, A. A., & Parnell, C. E. 2011, SoPh, 272, 29
Miesch, M. S., & Dikpati, M. 2014, ApJ, 785, L8
Mironova, I. A., Aplin, K. L., Arnold, F., et al. 2015, SSRv, 194, 1
Nesme-Ribes, E., Ferreira, E. N., Sadourny, R., Le Treut, H., & Li, Z. X. 1993, JGR, 98, 18923
Parnell, C. E. 2001, SoPh, 200, 23
Parnell, C. E. 2002, MNRAS, 335, 389
Parnell, C. E., DeForest, C. E., Hagenaar, H. J., et al. 2009, ApJ, 698, 75
Réville, V., Brun, A. S., Strugarek, A., et al. 2015, ApJ, 814, 99
Rieutord, M., & Rincon, F. 2010, LRSP, 7, 2
Riley, P., Lionello, R., Linker, J. A., et al. 2015, ApJ, 802, 105
Scherrer, P. H., Schou, J., Bush, R. I., et al. 2012, SoPh, 275, 207
Schrijver, C. J. 2001, ApJ, 547, 475
Schrijver, C. J., & DeRosa, M. L. 2003, SoPh, 212, 165
Schrijver, C. J., DeRosa, M. L., & Title, A. M. 2002, ApJ, 577, 1006
Schrijver, C. J., Title, A. M., van Ballegooijen, A. A., Hagenaar, H. J., & Shine, R. A. 1997, ApJ, 487, 424
Simon, G. W., & Leighton, R. B. 1964, ApJ, 140, 1120
Solanki, S. K. 2003, A&ARv, 11, 153
Švanda, M., Brun, A. S., Roudier, T., & Jouve, L. 2016, A&A, 586, A123
Svensmark, H., & Friis-Christensen, E. 1997, JASTP, 59, 1225
Thibault, K., Charbonneau, P., & Béland, M. 2014, ApJ, 796, 19
Thibault, K., Charbonneau, P., & Crouch, A. D. 2012, ApJ, 757, 187
Thornton, L. M., & Parnell, C. E. 2011, SoPh, 269, 13
Usoskin, I. G. 2013, LRSP, 10, 1
Usoskin, I. G., Kananen, H., Mursula, K., Tanskanen, P., & Kovaltsov, G. A. 1998, JGR, 103, 9567
Usoskin, I. G., & Kovaltsov, G. A. 2008, CRGeo, 340, 441
Usoskin, I. G., Mursula, K., & Kovaltsov, G. A. 2001, JGR, 106, 16039
van Driel-Gesztelyi, L., & Green, L. M. 2015, LRSP, 12, 1
Wang, Y.-M., Lean, J. L., & Sheeley, N. R., Jr. 2005, ApJ, 625, 522
Wang, Y.-M., Nash, A. G., & Sheeley, N. R., Jr. 1989a, ApJ, 347, 529
Wang, Y.-M., Nash, A. G., & Sheeley, N. R., Jr. 1989b, Sci, 245, 712
Wang, Y.-M., & Sheeley, N. R., Jr. 1991, ApJ, 375, 761
Yeates, A. R., Mackay, D. H., & van Ballegooijen, A. A. 2008, SoPh, 247, 103
Yeates, A. R., Mackay, D. H., van Ballegooijen, A. A., & Constable, J. A. 2010, JGR, 115, A09112
Zhou, G. P., Wang, J. X., & Jin, C. L. 2010, SoPh, 267, 63